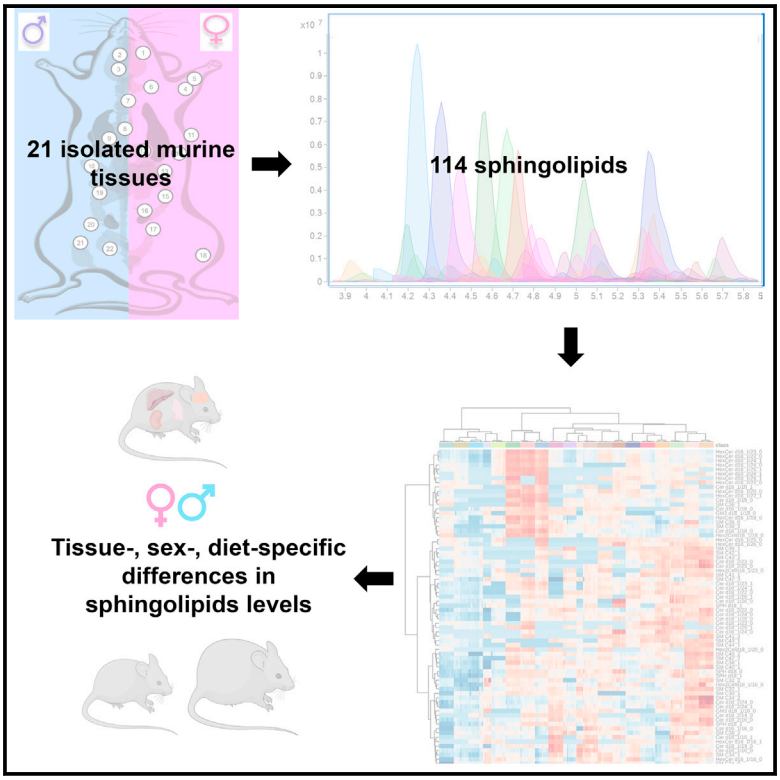
Cell Reports

Resource

A reference map of sphingolipids in murine tissues

Graphical abstract



Authors

Sneha Muralidharan, Mitsugu Shimobayashi, Shanshan Ji, Bo Burla, Michael N. Hall, Markus R. Wenk, Federico Torta

Correspondence

bchmrw@nus.edu.sg (M.R.W.), bchfdtt@nus.edu.sg (F.T.)

In brief

Sphingolipids are involved in numerous cellular processes, but a systematic and comprehensive map of their tissue distribution is missing. Using targeted lipidomics, Muralidharan et al. provide quantitative and qualitative profiles of 114 sphingolipid species across 21 murine tissues, highlighting their variation as a function of sex and diet.

Highlights

- Sphingolipids atlas of 21 tissues from C57BL/6 mice
- Quantitative differences of sphingolipids across tissues
- Sex-specific differences in the sphingolipidome of 21 mouse tissues
- Effect of high-fat diet on the sphingolipidome

Muralidharan et al., 2021, Cell Reports *35*, 109250
June 15, 2021 © 2021 The Authors.
https://doi.org/10.1016/j.celrep.2021.109250

CellPress

Cell Reports

CellPress
OPEN ACCESS

Resource

A reference map of sphingolipids in murine tissues

Sneha Muralidharan,[1,2] Mitsugu Shimobayashi,[3] Shanshan Ji,[2] Bo Burla,[2] Michael N. Hall,[3] Markus R. Wenk,[2,4,*] and Federico Torta[2,4,5,*]

[1]Department of Biological Sciences, National University of Singapore, 16 Science Drive 4, Singapore 117558, Singapore
[2]Singapore Lipidomics Incubator, Life Sciences Institute, National University of Singapore, Singapore 117456, Singapore
[3]Biozentrum – Center for Molecular Life Sciences, University of Basel, 4056 Basel, Switzerland
[4]Department of Biochemistry, Yong Loo Lin School of Medicine, National University of Singapore, 28 Medical Drive, Singapore 117456, Singapore
[5]Lead contact
*Correspondence: bchmrw@nus.edu.sg (M.R.W.), bchfdtt@nus.edu.sg (F.T.)
https://doi.org/10.1016/j.celrep.2021.109250

SUMMARY

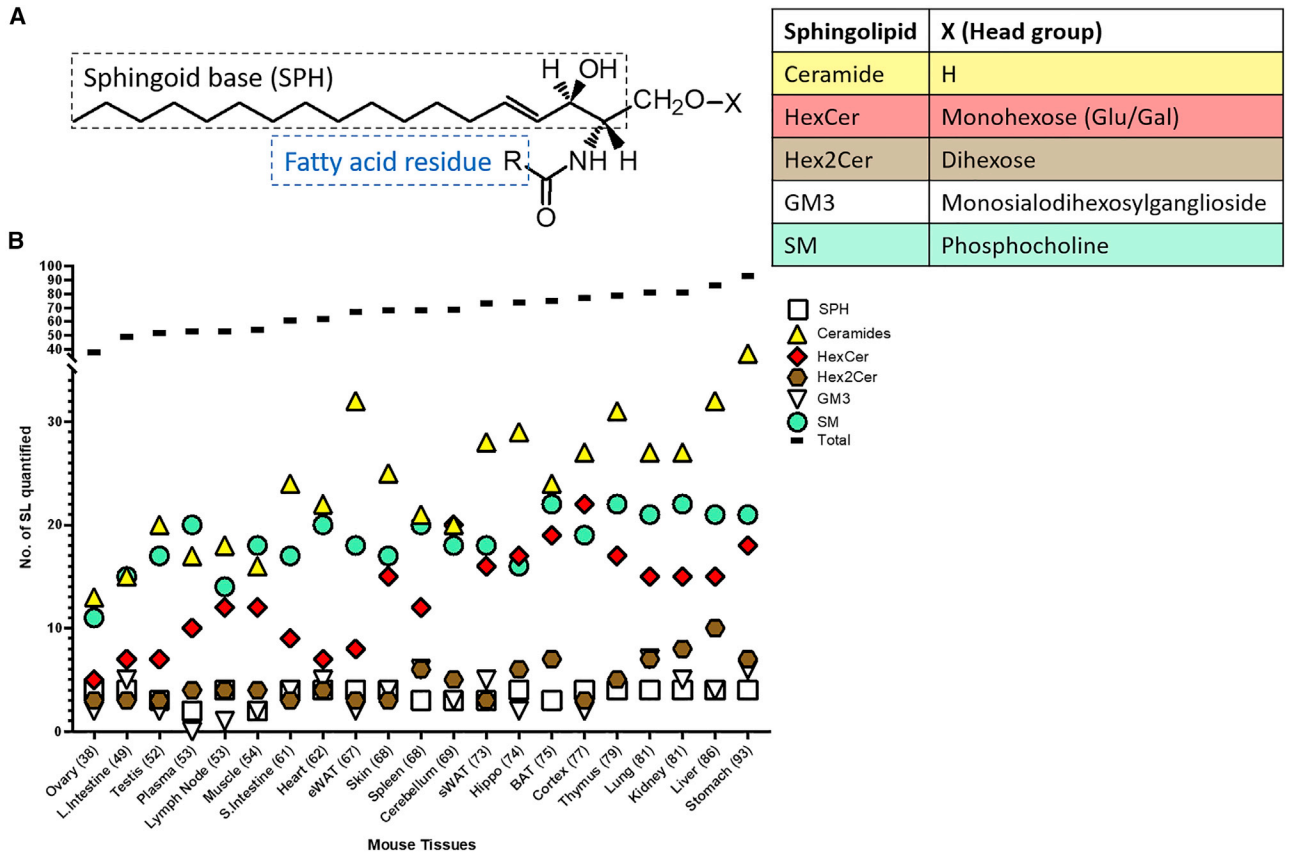
Sphingolipids (SPs) have both a structural role in the cell membranes and a signaling function that regulates many cellular processes. The enormous structural diversity and low abundance of many SPs pose a challenge for their identification and quantification. Recent advances in lipidomics, in particular liquid chromatography (LC) coupled with mass spectrometry (MS), provide methods to detect and quantify many low-abundant SP species reliably. Here we use LC-MS to compile a "murine sphingolipid atlas," containing the qualitative and quantitative distribution of 114 SPs in 21 tissues of a widely utilized wild-type laboratory mouse strain (C57BL/6). We report tissue-specific SP fingerprints, as well as sex-specific differences in the same tissue. This is a comprehensive, quantitative sphingolipidomic map of mammalian tissues collected in a systematic fashion. It will complement other tissue compendia for interrogation into the role of SP in mammalian health and disease.

INTRODUCTION

Describing the molecular components of animal tissues is crucial for the understanding of biology and disease. To date, most of the efforts have focused on the characterization of the tissues, RNA, or protein components (Huttlin et al., 2010; Palasca et al., 2018; Su et al., 2004; Uhlén et al., 2015), and only recently, detailed profiling of metabolites showed a more direct connection with phenotypes, providing important complementary information to previous studies. As an important class of metabolites, lipids exhibit enormous structural and functional diversity. They are essential architectural components of the cells where they mediate interactions with and between proteins. These interactions trigger many lipid-based signaling pathways and regulate membrane trafficking, cell growth, and survival (Cho and Stahelin, 2005). Recently, mass spectrometry (MS)-based measurements have been used to generate maps of the distribution of lipids in rodent tissues (Jain et al., 2014; Pradas et al., 2018).

Sphingolipids (SPs) represent only one among the eight categories in which lipids are classified (Fahy et al., 2005, 2009), and they are characterized by the presence of a sphingoid base (SPH) as a structural backbone. SPs play important roles in all major aspects of cell biology (Hannun and Obeid, 2018), including cell growth, cell cycle, cell death (Spiegel and Merrill, 1996), adhesion and migration (Adada et al., 2015; Canals et al., 2012), inflammation (Spiegel and Milstien, 2011), angiogenesis (Li et al., 2011), response to stress, and autophagy (Harvald et al., 2015). Dysregulated SP levels are involved in the development of obesity, insulin resistance, diabetic pro-inflammatory states, and cardiovascular and non-alcoholic fatty liver diseases (NAFLDs) (Régnier et al., 2019; Russo et al., 2013a). Monogenic defects of SP biosynthesis have been identified in humans, and they manifest mainly as neurological or skin-related disorders. The clinical manifestations include inherited sensory and autonomic neuropathy (HSAN), epilepsy, paraplegia and ataxia, retinitis, and ichthyosis (Astudillo et al., 2015). The involvement of SPs in many different processes highlights their functional flexibility, possibly linked to their enormous structural diversity (Figure 1A). The majority of SPH backbones are amide linked with many different fatty-acyl moieties to form ceramides (Cers). Cers can then be modified to form glycosphingolipids (glycoSP) with either a single sugar moiety to generate monohexosylceramides (HexCers), two sugars to generate dihexosylceramides (Hex2Cers), or more than two, originating complex species, such as globo- and ganglio-sides (GM3). The head group of the Cers can also be modified to form sphingomyelins (SMs) or ceramide-1-phosphates (C1Ps). Even if present in low amounts, the biologically active phosphorylated lyso-sphingolipids, such as sphingoid base-1-phosphates (S1Ps), have extremely important signaling functions (Merrill, 2011). The diverse distribution of SPs in mammalian tissues has not yet been fully characterized, and the role of the various molecular species in different organs is not yet understood. A comprehensive SP analysis across tissues would represent a first step toward understanding their possible specific functions, as done previously for other

This is an open access article under the CC BY-NC-ND license (http://creativecommons.org/licenses/by-nc-nd/4.0/).



Sphingolipid	X (Head group)
Ceramide	H
HexCer	Monohexose (Glu/Gal)
Hex2Cer	Dihexose
GM3	Monosialodihexosylganglioside
SM	Phosphocholine

Figure 1. Sphingolipid subclasses analyzed in this study

(A) The sphingoid base (SPH) is the characteristic structural unit of all sphingolipids. Ceramides are formed when a fatty acid is attached to the SPH. The ceramide head groups can be modified with a phosphocholine to form sphingomyelins (SMs) or with a monohexosyl sugar moiety to form monohexosylceramides (HexCers) and dihexosyl sugars to form dihexosylceramides (Hex2Cers). Hex2Cers are precursors of more complex sphingolipids, such as gangliosides.

(B) Total number of sphingolipids quantified in each tissue. Symbols represent different sphingolipid subclasses. The dashed line represents the total number of SPs measured in each tissue.

molecular effectors, such as mRNA transcripts (Su et al., 2004) and proteins (Huttlin et al., 2010).

The utility of animal models to study the effects of a dysregulated sphingolipidome has been shown in multiple cases. Wigger et al. (2017) investigated changes of the murine plasma lipidome in response to metabolic stress, to find markers that could assess the risk for developing type 2 diabetes (T2D). A group of SPs that strongly correlated with insulin secretion and glucose tolerance across mouse strains was identified. In the same study, a targeted analysis of the same SPs in over 250 human individuals who developed T2D from two different prospective cohorts revealed that the plasma concentrations of dihydroceramide and ceramide species could predict T2D development up to 9 years earlier. Lysosomal storage diseases are another example where the use of murine models gave a better understanding of a human disease linked to a dysregulation of the SP pathway (Gómez-Grau et al., 2017; Schiffer et al., 2020; Taguchi et al., 2013). In particular, Fabry disease is an X-linked inherited disorder resulting from deficient activity of the lysosomal enzyme α-galactosidase A (α-Gal A). Glycosphingolipids with terminal α-linked galactosyl moieties accumulate in the liver, heart, spleen, kidney, vascular endothelial cells, and plasma of the patients, causing occlusive vascular disease of the heart, kidney, and brain and leading to premature mortality. Mouse models deficient in α-Gal A display a complete lack of activity and accumulate Gb3 (Hex3Cer) in the liver and the kidneys, indicating a similar pathophysiology as observed in patients with Fabry (Ohshima et al., 1997). Although many cases have shown similarities between the sphingolipidome of mice and humans, we need to highlight that differences are also present and relevant for the study of specific SP subclasses. As reported by Hornemann et al. (2009), it has to be considered that rodents and humans are distinct with respect to d16-sphingolipid metabolism, a fact that should be kept in mind when working with rodent models of a disease where d16 SP might play a relevant role, such as cardiovascular pathologies.

Our manuscript reports a description of the sphingolipidome of 21 murine tissues across genders that covers a total of 114 SP species. We provide here a detailed quantitative map of high- and low-abundant SP across organs, their correlations in different tissues, and a comparison between profiles obtained

from male and female mice, showing the presence of highly significant sex-related differences in certain organs. Hex2Cers, for example, showed striking differences in the kidneys of males and females (50-fold difference). Furthermore, we show that a high-fat diet (HFD) leads to generally increased levels of SP in plasma, liver, and adipose tissue with tissue-specific effects. Thus, our study provides hitherto unavailable information of SP distribution and degree of variation as a function of important variables, i.e., sex, tissue specialization, and diet.

RESULTS AND DISCUSSION

A rapid and simple approach to quantify the sphingolipidome of mouse tissues

To compile a quantitative and qualitative atlas of the mouse sphingolipidome, we report the relative abundance of SPs extracted from a similar amount (~30 mg) of 21 adult tissues of 5 male and 6 female C57BL/6 mice (Figures D1A–D1U in Data S1). The 21 murine tissues selected for this study included hippocampus, cerebellum, cortex, lung, heart, spleen, kidney, liver, stomach, large intestine, small intestine (SI), brown adipose tissue (BAT), subcutaneous white adipose tissue (sWAT), epididymal white adipose tissue (eWAT), testis, ovary, muscle (quadriceps), skin (isolated from the back), lymph node, thymus, and plasma. Snap-frozen tissues (~30 mg) were transferred to 2-mL homogenization tubes containing 1 mL BUME (butanol/methanol 1:1 with internal standards), and frozen tissues were homogenized within 60 s. The samples were sonicated for 30 min followed by centrifugation, to precipitate the proteins and other insoluble materials, and the supernatant was collected.

We applied a comprehensive targeted method, based on current literature (Haynes et al., 2009; Sullards et al., 2011; Wang et al., 2014), to enable the detection and quantification of 151 SP species, including rare and low-abundant species (containing SPH d16:1 and d18:2) that have not been measured in most of the previous publications. The function of these SPH variants has not yet been clarified, and few studies indicate non-overlapping biological roles for these lipids. For example, myristate-derived d16:1 SPs accumulate in obesity and can induce cell death (Russo et al., 2013b), while deoxysphingolipids (m18:0, m18:1) are elevated in metabolic syndrome and T2D (Zuellig et al., 2014). Isomers, such as Cers d18:1/24:1 and Cer d18:2/24:0, could be separated by chromatography and the SPH composition determined. At least two product ions were used for the identification of each single lipid, with the most abundant product ion being used as the quantifier. In a run time of 10.8 min, our UPLC-ESI/MS/MS method could measure up to 151 SP species. After data filtering based on quality control samples, the semiquantitative levels of a total of 114 SP species were reported across 21 tissues.

Our data represent the SP content in each organ as a whole, not in specialized cell types or tissue regions, which we recognize could be a limitation of our study. Another limitation of our study (but common to all lipidomic experiments) is that, due to the lack of appropriate stable-isotope standards for all lipid species, we used only one internal standard per lipid class, providing information as relative lipid abundance. The full dataset is available for tissues (Table D1 in Data S1) and plasma (Table D2 in Data S1).

Clustering mouse tissues based on their sphingolipidome reveals tissue-specific patterns

Our analysis profiled the distribution and structural diversity of SPs: the lowest number (38 SP species) was found in the ovary, while the highest (93 SP species) was in the stomach (Figure 1B, dashed line). We observed a wide overlap between the identified SP, but only 11 species were common to all the tissues (Table S1). This might suggest a housekeeping function for these species also because of their high relative abundance. The common lipids include sphingosine (SPH d18:1), which is the most abundant mammalian SPH. One of its known targets is protein kinase C, which is involved in cell-cycle regulation (Black and Black, 2013). The common Cers include Cer d18:1/16:0 and Cer d18:1/18:0, both of which affect insulin resistance (Bergman et al., 2016; Hla and Kolesnick, 2014; Tonks et al., 2016), and Cer d18:2/24:0 and Cer d18:2/24:1, whose function is unknown. The common SM species across all the 21 tissues were SM 32:1, SM 34:0, SM 34:1, and SM 34:2. Although the specific functions of each molecular species of SM is unknown, in general SMs are involved in the formation of lipid rafts, cell signaling, lipid and protein sorting, and membrane trafficking (Chakraborty and Jiang, 2013). Only four different SPs were found in single tissues: Cer d16:1/22:1 in liver, Cer d16:1/26:0 in stomach, Cer d16:1/26:1 in skin, and Hex2Cer d18:2/18:1 in hippocampus. The highest number of total different SP species (93 SPs) was observed in stomach, where the dietary contribution to the SP pool could be more relevant. SPs are constituents in small amounts of most foods. Once introduced inside the body, they are hydrolyzed in the gut to simpler components (Cers and SPHs) that are used by cells to regulate their functions (Duan and Nilsson, 2009). SMs and cerebrosides are hydrolyzed mainly in the small intestine and colon of rats and mice because of the presence of sphingomyelinase, glucoceramidase, and ceramidase activities. Sphingosines and Cers derived from complex sphingolipids are then degraded to fatty acids (FAs) or reincorporated into complex sphingolipids in the intestinal cells (Schmelz et al., 1994). When labeled SPs were fed to rats, they were retrieved in lymph, blood, and liver, suggesting that a part of dietary SP appears in the circulation (Johnson et al., 2020).

When considering all SPs, Cers showed the highest structural diversity among all tissues (13 species in ovary and 37 in stomach). A very heterogeneous pool of Cers, HexCers, Hex2Cers, and SMs was observed in stomach, cerebellum, liver, and plasma, respectively. In particular, the number of detectable HexCer species was significantly higher in all the brain regions due to their localized high abundance. None of the 114 SPs were present at the same level across tissues. Instead, all exhibited fold changes between 2 and 8,000 between the highest- and lowest-expressing tissues. The highest fold change was observed for HexCer d18:1/24:1, with its lowest level observed in eWAT (~4 nmol/g dry weight) and its highest in cerebellum (~30,000 nmol/g dry weight). We generated a relative comparison between tissues, using liver (one of the major contributors to circulating SPs) as a reference. Although the total SP level does not show significant variations, some SP species are

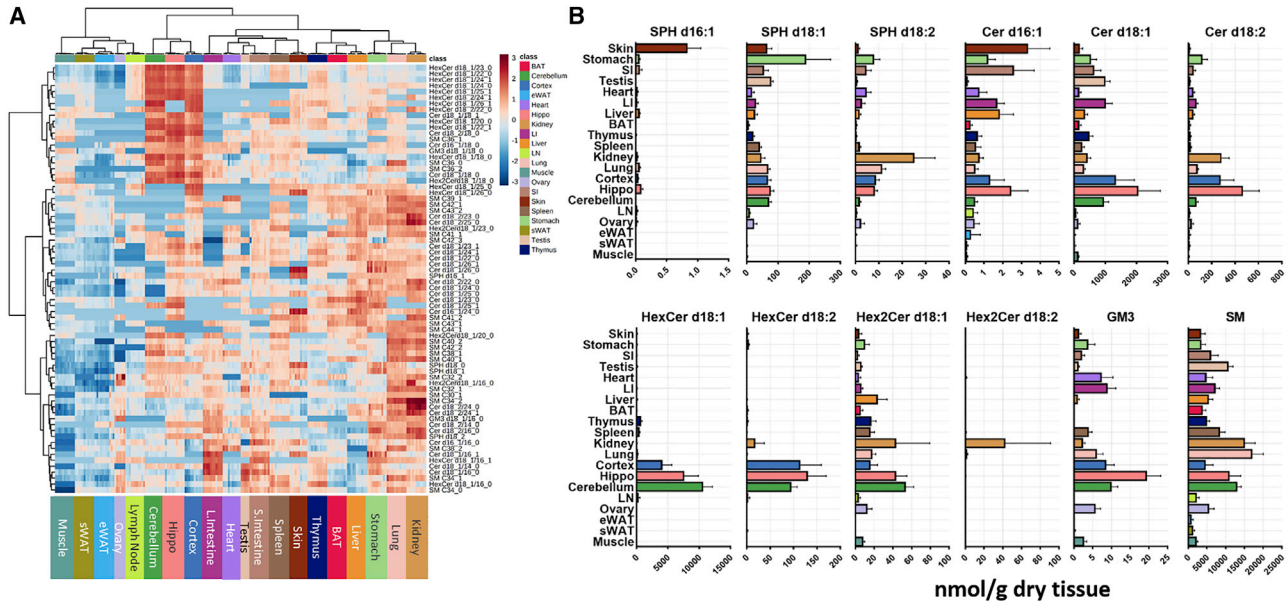


Figure 2. Tissue-specific patterns of sphingolipidome

(A) Heatmap of sphingolipid concentrations and distribution across the C57BL/6 mouse tissues. Each row represents levels of sphingolipid molecular species across tissues. The *Z* score value represents the normalized abundance of each lipid in arbitrary units. Each column represents a tissue and indicates the average of all the males (n = 5) and females (n = 6).

(B) Bar charts representing the average concentration in nanomoles (nmol) of lipid per gram (lipid/g) of dry tissue of representative sphingolipid subclasses in the analyzed tissues. Error bars represent the standard deviation across 11 mouse samples (5 males and 6 females).

extremely abundant in specific tissues (Figure D2 in Data S1). Glycosphingolipids show the highest variations in brain, supporting the idea of a tissue-specific function. In kidney we observed the highest fold changes for d18:2 containing SP, such as Cer d18:2/24:0, Cer d18:2/22:0, Cer d18:2/24:1, and SM 34:2. Stomach shows the highest fold changes for the very long-chain Cer d18:1/26:0, while in the intestine, the long-chain Cer d18:1/16:0 and Cer d18:1/18:0 are the most abundant. At the same time, some SP levels did not change significantly across the tissues (such as SM 42:1), suggesting a possible housekeeping function. In addition, we examined the variability between individual mice. Our data confirmed that the difference between tissue types exceeds the one between individuals (Figure S1).

Principal-component analysis of the levels of SP allowed a discrimination between the different tissues (Figure S1). In this representation, all the biological replicates and physiologically related tissues clustered together. Brain regions (cerebellum, cortex, and hippocampus) clearly segregated from the others; intestine, kidney, stomach, and lung were present as a separated cluster. When considering adipose tissues, eWAT and sWAT clustered together but separately from BAT. BAT was more similar to other tissue types (liver, thymus) when considering their SP content. This confirms that a similar lipid composition may arise in cell types from distinct developmental lineages (Jain et al., 2014).

We next performed hierarchical clustering analysis to derive more insights into similarities and differences of SP diversity across tissues (Figure 2A). We represented the level of 114 SPs as measured in our study and clustered them based on their relative abundance. This approach, previously used to discover the function of uncharacterized genes from gene expression patterns (Eisen et al., 1998), may also help elucidate the functions of SPs in tissues. It is interesting to notice the close clustering between skin, stomach, and intestines, where a similar lipid composition might be related to the barrier function of the tissues (for example, the presence of very long-chain FA, such as C26:0 containing SPs, might generate thicker membranes; Figure 3) and for a similar underlying reason, immune organs (spleen and thymus) were closely aligned (Figure 2A; Figure S1). WATs and BATs were well separated from each other because of their different SP levels, an observation that could be explained by their different morphology and metabolic activity (Rosell et al., 2014). Some of these differences include the presence of GM3 and C18:1 containing SPs in WAT (Figures D1B and D1C in Data S1) that are absent in BAT (Figure D1M in Data S1). The three brain regions clustered together reproducibly, confirming that a similar composition might be required to play a similar physiological task. In the hierarchical clustering analysis, the same tissues in males and females were always the closest, indicating that the SP composition had a more significant association to the tissue type than to animals' sex (data not shown).

To understand the quantitative distribution of SP, their relative concentration was represented by bar charts, as shown in linear scale (Figure 2B) and log scale (Figure D3A in Data S1), for 12 representative SP classes. Although the total SP concentration was clearly higher in the brain, followed by lung and kidney (Figure D3B in Data S1), we show here how the total amount of SMs was found to be equally distributed across tissues, despite its preponderant function in the myelin sheets of the nervous

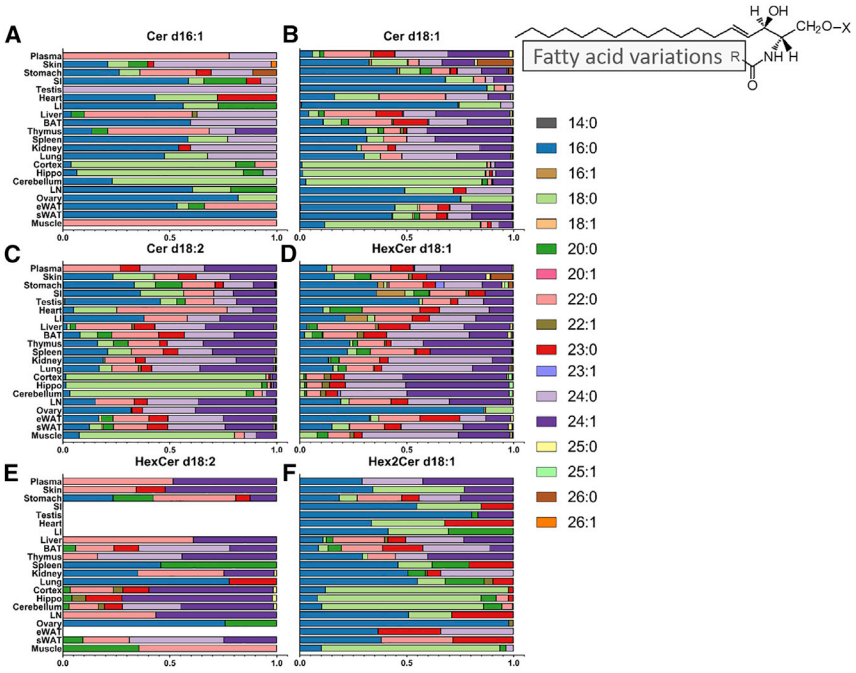


Figure 3. Distribution of long-chain bases and acyl chains between tissues and subclasses of sphingolipids

Relative abundance according to chain length and double-bond number of sphingolipids in 21 mouse tissues collected from 11 mice (5 males and 6 females). Each fatty-acyl chain length is indicated by a unique color, and the fatty-acyl composition is shown for (A) Cer d16:1, (B) Cer d18:1, (C) Cer d18:2, (D) HexCer d18:1, (E) HexCer d18:2, and (F) Hex2Cer d18:1. The x axis represents the relative abundance of each sphingolipid subclass.

system. Some molecular species showed a distinctive pattern of tissue abundance, which was not highlighted when lipid classes as a whole were analyzed. We have reason to believe the presence of high levels of a specific lipid in a tissue may provide an important hint about its functional role.

When considering SPHs, their total levels were higher in the stomach (Figure D3B in Data S1), although most of the dietary SP hydrolysis and absorption has been reported to happen in the intestinal tract (Vesper et al., 1999). However, the stomach shows the highest expression of the serine palmitoyltransferase small subunit B, which is one of the factors determining the substrate preference of serine palmitoyl transferase (SPT) complex, as reported in the public repository Genevestigator (Hruz et al., 2008) (Figure D4 in Data S1). The specific d16:1 SPH species showed a very characteristic peak value in skin (Figure 2B). The specific function of this SPH molecular species is not yet known, but it probably does not serve only as a precursor for the corresponding d16:1 Cers, which we found to have a comparable level in several tissues.

When Cers containing different backbones were considered, Cer d16:1 was indeed particularly abundant in skin, correlating with the high amount of its precursor, while Cer d18:1 and Cer d18:2 were higher in the hippocampus, the region of the brain containing the highest levels of total Cers (Figure 2B). Another subclass that shows a very typical distribution is the HexCer, which in the three brain regions is several orders of magnitude higher than in all the other tissues (Figure 2B; Figure D3B in Data S1) and represents 89% of the total HexCers measured, independently of their SPH backbone. This observation is also explained by the fact that the levels of galactosylceramides (GalCers) are especially high in brain and have been reported to be higher than glucosylceramides (GluCers) in wild-type mouse brain (Boutin et al., 2016). Because our method could not chromatographically separate GluCers and GalCers, we reported their combined abundance. The extreme high level of this SP in brain, when compared with the other tissues, suggests a very specialized and important function of HexCers. Previous studies revealed that HexCers mediate signal transduction and cell adhesion and are crucial for the formation of nervous tissues (Yu et al., 2009). The total Hex2Cer levels (and for both d18:1 and d18:2 Hex2Cer) were instead higher in kidney (Figure 2B; Figure D3B in Data S1). GlycoSPs play a role in insulin resistance and diabetes, and recently their role in diabetic nephropathy (DN) has received more attention. In diabetic mouse models, HexCer and Hex2Cer are elevated in kidney, specifically in glomeruli (Subathra et al., 2015). In these models, type 2 diabetes has been shown to lead to accumulation of HexCers and Hex2Cers in renal tissue, resulting in fibrosis, extracellular matrix production, and hypertrophy. The function of Hex2Cer is probably linked to the stimulation of renal cell proliferation, affected in polycystic kidney disease (Chatterjee et al., 1996). One of the most promising therapies for DN is indeed based on the use of GluCer (HexCer) inhibitors (eliglustat), because glycoSP inhibition has been shown to cause growth arrest (Shayman, 2018).

Lung showed very high levels of SMs, the major SP in mammalian tissues (Figure 2B). Here, SMs are structural components of pulmonary surfactants and play a role in reducing the surface tension at the air-liquid interface of the lung (Veldhuizen and Haagsman, 2000). However, we also observed a different distribution between different types of SM. The saturated SMs were higher in lung, and the SM containing more than one double bond were higher in the kidney (Figure D3B in Data S1). The total GM3 concentration (Figure 2B) was higher in the hippocampus (as observed for the other glycoSP), indicating its critical role in neuronal and brain development (Palmano et al., 2015).

Distribution of long-chain bases and acyl chains between tissues and subclasses of SP

The two main structural constituents of SP determining diversity are the (1) long-chain backbone and (2) the fatty-acyl chains (Figure 1A). We analyzed how these two components are distributed along tissues and subclasses. Based on the fatty-acyl distribution (Figures 3A–3C; Figures S2A–S2C), C18:0 is the main

component of brain Cers in cerebellum, cortex, and hippocampus. This could be explained by the high expression level of ceramide synthase 1 (CerS1) in the brain (data for SP gene expression from mouse tissues obtained from Genevestigator is shown in Figure D5 in Data S1), an enzyme that exhibits a preference for C18 acyl coenzyme A (CoA) (Laviad et al., 2008). This particular ceramide might have a more relevant function in brain because it is the relatively highest species only in this tissue, whereas Cers containing C16 and C24 FA are the most abundant in all the others. We hypothesize that tissue-specific distributions of molecular species could aid in the identification of circulating markers, indicating the damage of a specific organ through their release into circulation. A few studies have shown that the SP levels in plasma, such as SM/ceramide ratios, could serve as blood-based biomarkers to predict the progression of Alzheimer's disease after their release from brain (Mielke et al., 2011; Savica et al., 2016). We could then hypothesize that significant variations of levels of Cer containing C18:0 in spinal fluid might be predictive of pathologies connected to brain damage.

When comparing the FA distribution in the Cers with different backbones, we noticed that d16:1 Cers are enriched in longer FA (C > 20), a possible steric compensation for the shorter SPH (Russo et al., 2013b). This might then suggest a preferred interaction between the CerS4 enzyme and d16 backbones, although this was never documented before. Cers containing d18:2 are quite similar to the most abundant d18:1 in terms of FA content, with probably a slight preference for longer FA (C24). We observed higher relative levels of Cer d18:2 in the kidney (Figure 2B), in agreement with previous literature (Jojima et al., 2020).

Glycosphingolipids are the most diverse SP subclass. They derive from a combination of multiple sugar moieties and different Cers, exhibit diverse functions, and can act as antigens, mediators of cell adhesion, and modulators of signal transduction (Hakomori, 2003). In developing brains, glycosphingolipids are suggested to play important roles in the nervous system formation (Yu et al., 2009). When looking at the relative abundance of different HexCers (Figures 3D and 3E; Figures S2D and S2E), it is interesting to notice a lack of correspondence, in terms of FA composition, with their direct precursors (Cers). This is particularly evident in the brain, where the most abundant Cers contain a C18 FA, while the most abundant HexCers contain longer chains (C > 20). The same observation was reported in beef brains, where the Cers contain more stearic acid (C18:0) and less of the longer-chain FAs (C > 20) when compared with HexCers (O'Brien and Rouser, 1964). Probably the Cers containing C16 and C18 are not converted to a stable form of HexCer but instead to Hex2Cer, as d18:1/16:0 and d18:1/18:0 are still the most abundant form of Hex2Cer in all the tissues. No significant differences were found between the FA composition of HexCers containing d18:1 and d18:2 backbones, suggesting a lack of preference of the glycosylating enzyme toward these SPH components of the ceramide.

The composition of specific FAs in each subclass might be a parameter to monitor during diet-related studies, where, for example, food rich in saturated FA (SFA) might also affect the SP composition and their function in tissues. Examples have been shown in humans (Luukkonen et al., 2018; Rosqvist et al., 2019) where SFA induced significant changes in all the SP subclasses in liver and blood plasma when compared with a PUFA-rich diet. In such studies, our atlas can represent the reference condition for mice fed with a regular chow-based diet. Because more complex glycoSPs, such as Hex3Cer and Hex4Cer, were not measured for this atlas, it will be the aim of future studies to check the quantitative structural relationship with their precursors.

SPHs and S1Ps

SPHs are the precursors of Cers and the product of their degradation, catalyzed by ceramidases. In Figure S3A, the representation of the content of SPH in all the tissues confirms a prevalence of the d18:1 form, followed by d18:0 and d18:2. With our analytical approach, the very low-abundant d16:1 SPH could be detected only in skin. The concentration of d16:1 SPH and the expression of the gene involved in its synthesis, SPTLC3, were indeed reported to be much lower in mice than in humans, complicating their detection (Russo et al., 2013b). The relative proportion between the different SPHs was quite conserved between tissues, with a highest proportion of d18:2 in kidney (Figure S3A), supporting the data reported for complex SP species in the same tissue. SPH can be phosphorylated to S1P, the final product of the SP pathway before degradation. S1P can play signaling functions by binding to cell surface receptors. This event is associated with a wide variety of physiological processes, such as vascular development, central nervous system homeostasis, and lymphocyte biology (Garris et al., 2014). There are five S1P receptors (S1PR1–5) whose functions are not yet fully clarified, for which the different S1P molecular species can have different specificity (Troupiotis-Tsaïlaki et al., 2017). A map of the abundance of S1P molecular species in 16 tissues (S1P could not be detected in other tissues) is shown in Figures S3B and S3C. We suggest that a correlation between the expression levels of S1PRs and the different molecular species of S1P abundance in the analyzed tissues might help in understanding if specific binding between S1Ps and S1PRs can happen physiologically. When detectable, the highest levels of S1P were found in the brain, while the lowest were measured in skin, BAT, and liver (Figure S3C). Recently, Kharel et al. (2020) demonstrated in murine models that indeed the liver is the primary site for clearance of S1P from the blood. According to this model, blood S1P is converted, via a cell surface phosphatase, to sphingosine at the hepatocyte surface. Sphingosine is then absorbed and converted again (via sphingosine kinase 2) to S1P, which is irreversibly degraded by the cellular lyase. After the brain, the tissue with the highest level of S1P was the lung, where these molecules have been shown to regulate the immune response and provide protection against pathogenic viruses, such as influenza (Zhao et al., 2019), by binding to S1PR1 on the endothelial cells surface and triggering the activation of a cytokine storm during infection (Teijaro et al., 2011). Indeed, the gene expression levels of S1PR1 and S1PR5 were high in brain, and S1PR1, S1PR2, and S1PR3 also showed high expression in the lung (Figure D5 in Data S1). We confirmed that S1P d18:1 is the most abundant form in all the tissues, with no significant difference between males and females. S1P d18:2, whose function is still unknown, is particularly abundant in kidney and

was not detected in stomach and intestine; this might suggest that S1P d18:2 or its precursors are not mainly absorbed from the diet, and also because of its absence in the skin, the hypothesis of a significant microbial contribution to its synthesis is not supported. The enzyme that adds the second unsaturation to the SPH has indeed been very recently identified as FADS3 (Jojima et al., 2020; Karsai et al., 2020). Based on analysis from existing RNA abundance data, the expression of FADS3, influenced by sex, is higher in the lung and kidney, supporting our findings for d18:2 containing SP. Other tissues showed a decreasing abundance of FADS3 in the order brain > intestine > stomach > liver (Jojima et al., 2020; Karsai et al., 2020; Pédrono et al., 2010), in agreement with our results shown for SPH d18:2 in Figure 2B.

Brain, lung (in which the expression of sphingosine kinase 1 is higher than in the other tissues; Fukuda et al., 2003), SI, and stomach showed particularly high levels of S1P.

Other rare S1P species were identified in some specific tissues. S1P d16:1 was found in the plasma, muscle, and BAT. Its absence in skin might suggest that its abundant precursor, SPH d16:1, is not efficiently phosphorylated in this tissue. S1P d17:1 was found in plasma, and its relative abundance was particularly high in skin. Because odd chain lipids are usually less abundant in mammals, the presence of S1P d17:1 (possibly containing a branched chain) might have originated from the microbiome normally present on the skin. S1P d20:1, otherwise present in the stomach, intestine, and muscle, was mainly concentrated in the brain. It has been demonstrated that the synthesis of this longer form of SPH is mainly due to the activity of the subunit SPTssb in the SPT complex. This subunit facilitates the use of stearoyl-CoA as a substrate, a component present at high concentrations also in Cer and HexCer containing C18 FA in brain. Data indicate a distinct functional relevance of SP with C20-SPH, and their accumulation can cause compromised neural and retinal functions (Zhao et al., 2015). The function of S1P d20:1 was not clear until very recently, when it was shown to block the S1P d18:1-induced COX-2 expression mediated via S1P2 activation in the nervous system of murine models (Vutukuri et al., 2020). This discovery might suggest an important role as pathway modulator for the different existing forms of S1P also in other tissues.

Sex-based differences

Sex-based differences have been widely recognized in epidemiology and affect outcomes of disorders in humans. Pathologies such as diabetes, renal disease, and cardiovascular disease are clearly influenced by sex (Regitz-Zagrosek et al., 2016; Kautzky-Willer et al., 2016; Martín-Timón et al., 2014). For example, women are more likely to suffer from autoimmune diseases (Ngo et al., 2014), while men are more prone to develop renal complications (Iseki, 2008). Despite research clearly showing that sex matters in animal research, many studies continue to be done in only males or females, to limit complexity and cost. The bias toward using only animals of one sex is often based on quite practical concerns, such as size of the animal and behavior. Many sex differences appear to be organ specific; therefore, the organ-specific metabolites content must be described for males and females. The same is true for circulating lipids. Sales et al. (2016) established that sex affects significantly the lipidome composition, shaped by hormonal contraceptives and mediated by sex hormone-binding proteins, suggesting that lipidomics epidemiological studies should consider sex-based sub-cohorts. In another recent study (Beyene et al., 2020), high-throughput lipidomics in two human cohorts identified sex-specific associations of lipid species with obesity. Because sex-related differences in lipid metabolism have been reported (Baars et al., 2018; Palmisano et al., 2018; Wang et al., 2011), we used our targeted approach to gain a deeper insight into the sex-specific SP profile of all the tissues we analyzed.

When comparing the lipid content from the same tissue between male and female mice, we found that the similarity was always higher than for different tissues in mice of the same sex (hierarchical clustering, analysis not shown). However, a PCA analysis identifying homogeneous groups within the same tissue was able to clearly separate male from female animals (Figure S4). When we conducted a t test to confirm sex-dependent compositional changes, five tissues (lung, kidney, skin, liver, BAT) showed significant differences (Figure 4). Kidney showed the biggest difference between males and females, mainly driven by the Hex2Cer levels. It is known that gender influences chronic kidney disease progression in humans, which is faster in males than in females (Carrero, 2010). The discovery of specific molecular signatures, in this case, the relative concentration of glycoSP, could suggest possible pathways and enzymatic reactions to target with therapies. SM species showed significant differences between males and females in the liver (Figure 4; Figure D1N in Data S1), with females showing higher levels. Previously, neutral sphingomyelinase-2 deficient (*fro/fro*) mice showed increased gender- and age-specific liver tumor formation, because tumors were formed only in aged males (*fro/fro*), but not females (Zhong et al., 2018). We can then hypothesize that a lower level of SM in male mouse liver must be under tight control. In skin and BAT, these differences are more distributed and affect different types of subclasses. Sex-specific differences were previously reported for lipids in BAT (although WAT did not show significant dimorphism) and mainly observed in triglycerides and phospholipids (Hoene et al., 2014). We report here that glycoSP and SM are present at a much higher concentration in BAT of females (Figure D1M in Data S1), probably influencing their ability to better adjust thermogenesis, according to a different morphological structure of the membranes in mitochondria (Kim et al., 2016).

SPs in blood plasma

Many studies on murine models make use of plasma as a primary readout for conditions or treatments, a representation of the relative abundance of SP subclasses in mouse plasma (Figure D1U in Data S1). We detected and quantified 55 SPs. The most abundant category was represented by SMs, followed by glycosphingolipids, Cers, and SPHs. Although SMs contain mostly FAs with 16 and 24C at comparable levels, in Cer and glycoSP there is a dominance of species containing either 22 or 24C FA. We also noticed a clear influence of sex on the content of FA 22:0, always present at a higher concentration in all SPs in males (Figure 4; Figure D1U in Data S1). Previous studies on relative

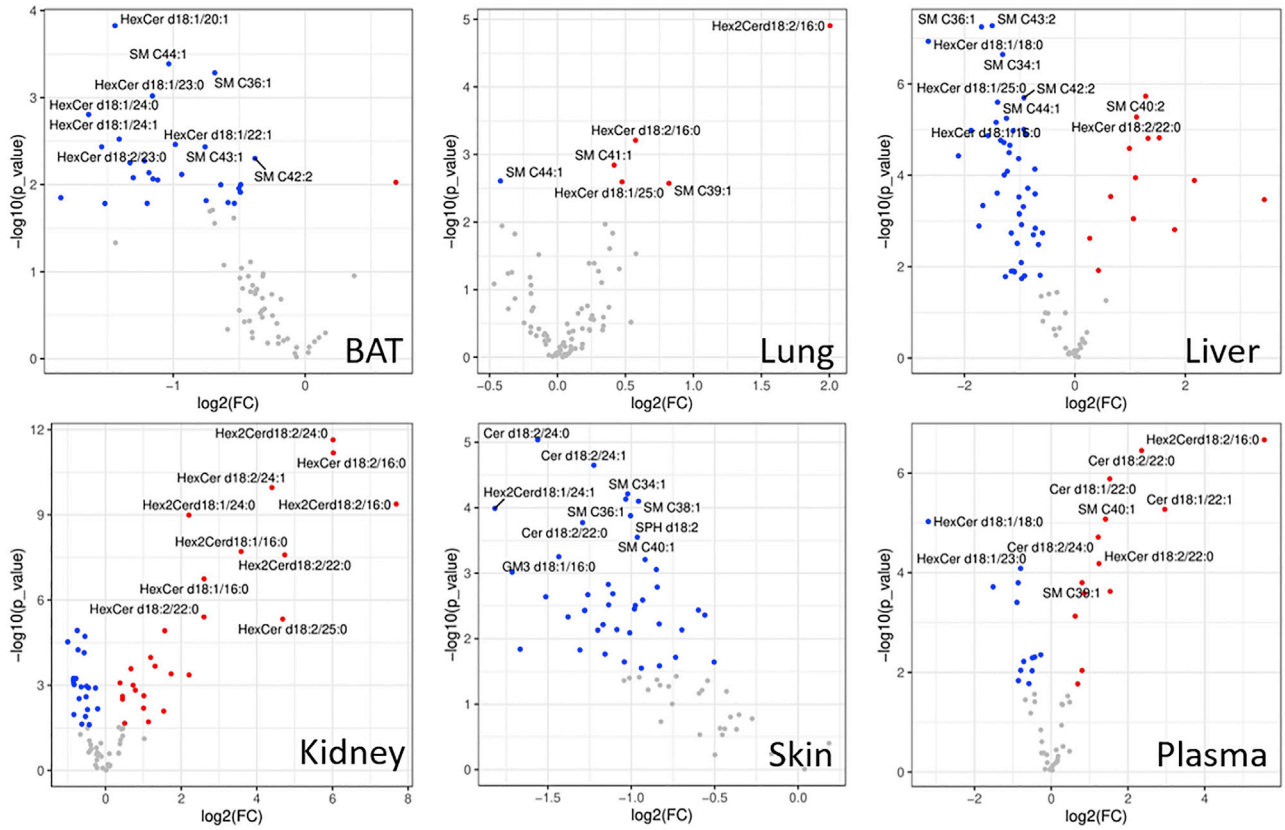


Figure 4. Sphingolipids showed significant sex-related differences in specific tissues

Each graph represents a different tissue, and lipids showing a significant ($p < 0.05$) fold change are indicated in color: lipids in blue are higher in females (n = 6), and lipids in red are higher in males (n = 5). The x axis represents the log2 fold change between males and females. Glycosphingolipids in kidney showed the highest sex-based difference. BAT, brown adipose tissue.

levels of plasma SP in C57BL/6 mice (Fox et al., 2011) reported relative SP levels well in agreement with our findings. However, when we compare the concentrations, there are also some discrepancies: whereas the Cer and SM levels were almost double in our study, HexCer and Hex2Cer were half of the levels previously reported in another publication (Giles et al., 2017). These discrepancies might be because of the limited comparability of relative quantitation and other factors, such as the number of species used to calculate the total Cer, the use of different internal standards (ISTD) and lipid extraction protocols (analytical factor), or different environmental conditions. The comparison between different datasets certainly will be improved in the near future, thanks to ongoing initiatives that promote the harmonization of lipidomic results through the use of reference materials (Triebl et al., 2020) and more complex internal standard mixtures. When comparing the plasma SP relative levels with the other tissues, the liver exhibited a similar pattern in terms of molecular composition, where Cers and glycoSPs with 22 and 24C FAs are the most abundant and where 16 and 24C FAs are higher in SMs. Liver was also the only tissue showing higher levels of 22:0 Cer in males, the same profile found in plasma.

Using the SP composition in mouse plasma as a baseline and based on the specific profile of each tissue, our data might be used to hypothesize the potential origin of a sudden increased level of specific SP in plasma in a pathological state. As an example, we can consider the circulating concentrations of specific TAG species in fatty liver disease models. Because TAGs are unusually high in livers of patients with NAFLD, a subset of them has been used as a circulating biomarker of that condition (Barr et al., 2010; Mayo et al., 2018). Based on our results (Figure S2E), a collection of tissue-specific high-abundant lipids, such as HexCer d18:2/16:0 in kidney, might be measured in plasma when a specific organ is injured (causing the release of that specific molecule into circulation), to probe their possible use in plasma biomarker-based discovery.

Effect of a HFD on the sphingolipidome of wild-type mice

The SP pathway regulates many cellular signaling mechanisms that have been implicated in metabolic homeostasis, and its dysregulation is often associated with metabolic diseases in humans. SP levels are significantly affected in the presence of insulin resistance, obesity, and steatosis. In animal models, it has been shown that in more than 100 inbred strains of mice and using a systems genetics approach (Parks et al., 2013), gene-by-diet interactions were found in loci associated with obesity traits. Association analysis with body fat percent increase (after 2 weeks of HFD) identified genome-wide significant loci that included Sptlc3, a subunit of SPT, the enzyme catalyzing the first

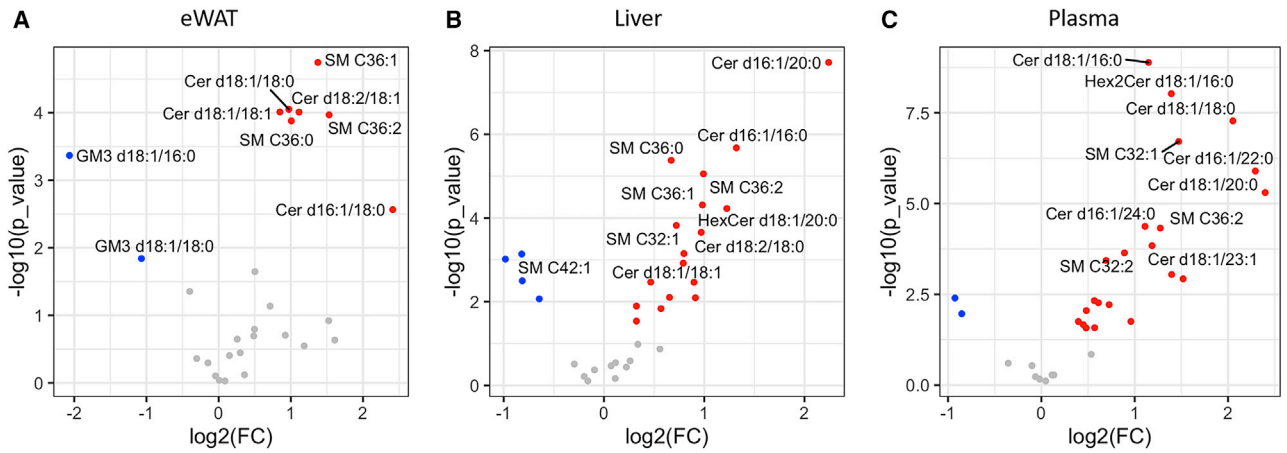


Figure 5. Effect of a high-fat diet (HFD) on the sphingolipidome of wild-type mice

Volcano plot representing the sphingolipidome changes in (A) eWAT, (B) liver, and (C) plasma collected from mice that were fed with either HFD (n = 8) or chow diet (n = 8). Significant lipids ($p < 0.05$) are indicated in color: lipids in red are higher in HFD-fed mice, and lipids in blue are lower in HFD-fed mice. Only the SP species that were reproducibly measured in all the experiments and those that passed our quality control filters were included. The x axis represents the log2 fold change.

irreversible step of the SP synthetic pathway. In the same publication, the authors also found that eight genome-wide significant loci were associated with body fat percentage growth after 8 weeks of HFD. Interestingly, the most significant signal was associated to Degs1, the desaturase that generates Cers, and its expression in adipose tissue strongly correlated with the body fat percentage.

We describe here the effect of a HFD on the sphingolipidome of three representative tissues (eWAT, liver, and plasma) in WT C57BL/6 mice. We observed that the levels of the majority of SPs increased in the tissues of mice fed with HFD, except for three SM and two GM3 species (Figure 5). A higher number of molecular species showed significant changes in plasma (25 SPs) and liver (21 SPs) when compared with eWAT (9 SPs), showing a more immediate effect on the blood-liver system and a higher resilience to changes of the adipose tissue. More specifically, HFD significantly increased the levels of most of the ceramide species, which have been shown to have a toxic/predictive effect in the development of cardiovascular and metabolic diseases in humans (Laaksonen et al., 2016; Meikle and Summers, 2017). When considering glycosphingolipids, we detected increased levels of HexCer and Hex2Cer in liver and plasma, but not at a level comparable with Cers. We also observed increased levels of C32 and C36 SM, while the levels of longer-chain SM (C42–44) were reduced in liver. This might be explained by high concentrations of short SFAs in the HFD food that are then incorporated into SPs by the animal tissues. The molecular species that showed a significant diet-dependent increase in this study have been previously linked to human pathologies developed after a prolonged exposure to unhealthy diets. As shown by others, the accumulation of C16 Cers can cause mitochondrial fragmentation and promote steatosis in obese individuals (Hammerschmidt et al., 2019), while increase in d18:1 Cers has been associated with alterations in the cell membrane structure, triggering insulin resistance (Chaurasia et al., 2019). We then compared the fold change induced by the HFD in each SP species between the three tissues. Figure S5 shows that fold changes in plasma showed a higher correlation with changes in liver when compared with eWAT, supporting the idea that, under HFD, measuring SP concentrations in plasma might reveal what is accumulating in the liver, avoiding more invasive techniques for sample collection. However, contributions of residual blood in liver tissue because of the absence of perfusion processes cannot be fully ruled out and thus might affect this interpretation. In general, the presence of a higher number of lipids above the identity line in Figure S5 indicates that changes in plasma are more pronounced than in the other tissues. We explain this observation with the fact that plasma composition is probably affected more rapidly and by the contribution from a multitude of other tissues that were not analyzed here.

Use of these data for future studies

All the data reported here are now publicly available on Mendeley Data (https://dx.doi.org/10.17632/gbgm9bscph.1). As the interest and need for lipidomic data are rapidly increasing in many fields, we will work on making our data available to the research community through other channels too. The main purpose of our work was to generate a reference database for comparison of the SP levels obtained from different tissues, models, and techniques, and we foresee the utility of our data for scientists in related fields. For example, the Metaspace platform (https://metaspace2020.eu) hosts an engine for metabolite annotation of imaging MS data from different tissues and origin, as well as a spatial metabolite knowledgebase of the metabolites from hundreds of public datasets provided by the community. Although METASPACE is based on high-resolution imaging MS, and our data were obtained using LC-MS/MS on low-resolution instruments, we believe our dataset will be a complementary reference for those users interested in a relative comparison between results obtained by different methods from the same mouse organs. We believe the possibility of integrating our dataset also with others obtained with a different approach will expand its utility.

Conclusions

A deeper knowledge of the metabolites content of mammalian tissues can help to identify biological mechanisms, molecular functions, biomarkers for disease, and targeted treatments. Most of the studies in this field are still made in model systems. Here we have described the sphingolipidome of 21 tissues from healthy wild-type mice, both males and females, as a reference for future studies. The SP distribution varies qualitatively and quantitatively across tissues. We observed that functionally related tissues (such as cerebellum, cortex, and hippocampus in brain) exhibit a similar sphingolipidome that drives the clustering between tissues. We foresee that the presence of tissue-specific SP will give insights into the possible mechanisms of specific diseases, generating the basis for new research. We also report that several tissues show significant differences between males and females, providing a resource for the study of SP-related pathologies that affect in different ways male and female humans. Because the total levels of SP in the body can be affected by diet, we reported the effects of 10 weeks of high-fat feeding on three tissues. In these conditions, we found a general increase in the SP levels and, in particular, of Cers that are known to mediate insulin resistance and inflammation. Because we found a good correlation between plasma and liver SPs in the high-fat feeding experiments, we concluded that measuring plasma levels of SP can quite reliably reflect their variation in hepatic tissue during such diet-induced perturbations. These results will provide a valuable resource to better understand the metabolism of human diseases.

STAR★METHODS

Detailed methods are provided in the online version of this paper and include the following:

- KEY RESOURCES TABLE
- RESOURCE AVAILABILITY
  - Lead contact
  - Materials availability
  - Data and code availability
- EXPERIMENTAL MODEL AND SUBJECT DETAILS
- METHOD DETAILS
  - Lipid extraction
  - Targeted lipidomics
  - Sphingoid base-1-phosphates (S1P) analysis
- QUANTIFICATION AND STATISTICAL ANALYSIS
  - LC-MS/MS data analysis
  - Normalization and quantification

SUPPLEMENTAL INFORMATION

Supplemental information can be found online at https://doi.org/10.1016/j.celrep.2021.109250.

ACKNOWLEDGMENTS

Work in SLING (S.M., S.J., B.B., M.R.W., F.T.) is supported by grants from the National University of Singapore via the Life Sciences Institute (LSI), the National Research Foundation (NRFSBP-P4), and A*STAR IAF-ICP I1901E0040. Some of the mouse images in the graphical abstract were derived from the Servier, CC0 CC-by-SA MIT License.

AUTHOR CONTRIBUTIONS

S.M., F.T., and M.R.W. designed the experiments and wrote the manuscript. M.S. and M.N.H. provided the mouse models and tissues and revised the manuscript. S.M. performed data acquisition and analysis. S.M., S.J., and B.B. performed statistical analysis and data visualization. F.T. and M.R.W. supervised the project.

DECLARATION OF INTERESTS

The authors declare no competing interests.

Received: January 7, 2021
Revised: April 21, 2021
Accepted: May 24, 2021
Published: June 15, 2021

REFERENCES

Adada, M.M., Canals, D., Jeong, N., Kelkar, A.D., Hernandez-Corbacho, M., Pulkoski-Gross, M.J., Donaldson, J.C., Hannun, Y.A., and Obeid, L.M. (2015). Intracellular sphingosine kinase 2-derived sphingosine-1-phosphate mediates epidermal growth factor-induced ezrin-radixin-moesin phosphorylation and cancer cell invasion. FASEB J. *29*, 4654–4669.

Alshehry, Z.H., Barlow, C.K., Weir, J.M., Zhou, Y., McConville, M.J., and Meikle, P.J. (2015). An Efficient Single Phase Method for the Extraction of Plasma Lipids. Metabolites *5*, 389–403.

Astudillo, L., Sabourdy, F., Therville, N., Bode, H., Ségui, B., Andrieu-Abadie, N., Hornemann, T., and Levade, T. (2015). Human genetic disorders of sphingolipid biosynthesis. J. Inherit. Metab. Dis. *38*, 65–76.

Baars, A., Oosting, A., Lohuis, M., Koehorst, M., El Aidy, S., Hugenholtz, F., Smidt, H., Mischke, M., Boekschoten, M.V., Verkade, H.J., et al. (2018). Sex differences in lipid metabolism are affected by presence of the gut microbiota. Sci. Rep. *8*, 13426.

Barr, J., Vázquez-Chantada, M., Alonso, C., Pérez-Cormenzana, M., Mayo, R., Galán, A., Caballería, J., Martín-Duce, A., Tran, A., Wagner, C., et al. (2010). Liquid chromatography-mass spectrometry-based parallel metabolic profiling of human and mouse model serum reveals putative biomarkers associated with the progression of nonalcoholic fatty liver disease. J. Proteome Res. *9*, 4501–4512.

Bergman, B.C., Brozinick, J.T., Strauss, A., Bacon, S., Kerege, A., Bui, H.H., Sanders, P., Siddall, P., Wei, T., Thomas, M.K., et al. (2016). Muscle sphingolipids during rest and exercise: a C18:0 signature for insulin resistance in humans. Diabetologia *59*, 785–798.

Beyene, H.B., Olshansky, G., Smith, A.A., Giles, C., Huynh, K., Cinel, M., Mellett, N.A., Cadby, G., Hung, J., Hui, J., et al. (2020). High-coverage plasma lipidomics reveals novel sex-specific lipidomic fingerprints of age and BMI: Evidence from two large population cohort studies. PLoS Biol. *18*, e3000870.

Black, A.R., and Black, J.D. (2013). Protein kinase C signaling and cell cycle regulation. Front. Immunol. *3*, 423.

Boutin, M., Sun, Y., Shacka, J.J., and Auray-Blais, C. (2016). Tandem Mass Spectrometry Multiplex Analysis of Glucosylceramide and Galactosylceramide Isoforms in Brain Tissues at Different Stages of Parkinson Disease. Anal. Chem. *88*, 1856–1863.

Canals, D., Roddy, P., and Hannun, Y.A. (2012). Protein phosphatase 1α mediates ceramide-induced ERM protein dephosphorylation: a novel mechanism independent of phosphatidylinositol 4, 5-biphosphate (PIP2) and myosin/ERM phosphatase. J. Biol. Chem. *287*, 10145–10155.

Carrero, J.J. (2010). Gender differences in chronic kidney disease: underpinnings and therapeutic implications. Kidney Blood Press. Res. *33*, 383–392.

Chakraborty, M., and Jiang, X.C. (2013). Sphingomyelin and its role in cellular signaling. Adv. Exp. Med. Biol. *991*, 1–14.

Chatterjee, S., Shi, W.Y., Wilson, P., and Mazumdar, A. (1996). Role of lactosylceramide and MAP kinase in the proliferation of proximal tubular cells in human polycystic kidney disease. J. Lipid Research *37*, 1334–1344.

Chaurasia, B., Tippetts, T.S., Mayoral Monibas, R., Liu, J., Li, Y., Wang, L., Wilkerson, J.L., Sweeney, C.R., Pereira, R.F., Sumida, D.H., et al. (2019). Targeting a ceramide double bond improves insulin resistance and hepatic steatosis. Science *365*, 386–392.

Cho, W., and Stahelin, R.V. (2005). Membrane-protein interactions in cell signaling and membrane trafficking. Annu. Rev. Biophys. Biomol. Struct. *34*, 119–151.

Chong, J., and Xia, J. (2020). Using MetaboAnalyst 4.0 for Metabolomics Data Analysis, Interpretation, and Integration with Other Omics Data. Methods Mol. Biol. *2104*, 337–360.

Chong, J., Soufan, O., Li, C., Caraus, I., Li, S., Bourque, G., Wishart, D.S., and Xia, J. (2018). MetaboAnalyst 4.0: towards more transparent and integrative metabolomics analysis. Nucleic Acids Res. *46* (*W1*), W486–W494.

Chong, J., Wishart, D.S., and Xia, J. (2019). Using MetaboAnalyst 4.0 for Comprehensive and Integrative Metabolomics Data Analysis. Curr. Protoc. Bioinformatics *68*, e86.

Duan, R.D., and Nilsson, A. (2009). Metabolism of sphingolipids in the gut and its relation to inflammation and cancer development. Prog. Lipid Res. *48*, 62–72.

Eisen, M.B., Spellman, P.T., Brown, P.O., and Botstein, D. (1998). Cluster analysis and display of genome-wide expression patterns. Proc. Natl. Acad. Sci. USA *95*, 14863–14868.

Fahy, E., Subramaniam, S., Brown, H.A., Glass, C.K., Merrill, A.H., Jr., Murphy, R.C., Raetz, C.R., Russell, D.W., Seyama, Y., Shaw, W., et al. (2005). A comprehensive classification system for lipids. J. Lipid Res. *46*, 839–861.

Fahy, E., Subramaniam, S., Murphy, R.C., Nishijima, M., Raetz, C.R., Shimizu, T., Spener, F., van Meer, G., Wakelam, M.J., and Dennis, E.A. (2009). Update of the LIPID MAPS comprehensive classification system for lipids. J. Lipid Res. *50* (*Suppl*), S9–S14.

Fox, T.E., Bewley, M.C., Unrath, K.A., Pedersen, M.M., Anderson, R.E., Jung, D.Y., Jefferson, L.S., Kim, J.K., Bronson, S.K., Flanagan, J.M., and Kester, M. (2011). Circulating sphingolipid biomarkers in models of type 1 diabetes. J. Lipid Res. *52*, 509–517.

Fukuda, Y., Kihara, A., and Igarashi, Y. (2003). Distribution of sphingosine kinase activity in mouse tissues: contribution of SPHK1. Biochem. Biophys. Res. Commun. *309*, 155–160.

Garris, C.S., Blaho, V.A., Hla, T., and Han, M.H. (2014). Sphingosine-1-phosphate receptor 1 signalling in T cells: trafficking and beyond. Immunology *142*, 347–353.

Giles, C., Takechi, R., Mellett, N.A., Meikle, P.J., Dhaliwal, S., and Mamo, J.C. (2017). Differential regulation of sphingolipid metabolism in plasma, hippocampus, and cerebral cortex of mice administered sphingolipid modulating agents. J. Neurochem. *141*, 413–422.

Gómez-Grau, M., Albaigès, J., Casas, J., Auladell, C., Dierssen, M., Vilageliu, L., and Grinberg, D. (2017). New murine Niemann-Pick type C models bearing a pseudoexon-generating mutation recapitulate the main neurobehavioural and molecular features of the disease. Sci. Rep. *7*, 41931.

Hakomori, S. (2003). Structure, organization, and function of glycosphingolipids in membrane. Curr. Opin. Hematol. *10*, 16–24.

Hammerschmidt, P., Ostkotte, D., Nolte, H., Gerl, M.J., Jais, A., Brunner, H.L., Sprenger, H.G., Awazawa, M., Nicholls, H.T., Turpin-Nolan, S.M., et al. (2019). CerS6-Derived Sphingolipids Interact with Mff and Promote Mitochondrial Fragmentation in Obesity. Cell *177*, 1536–1552.e23.

Han, X. (2016). Fragmentation patterns of sphingolipids. Lipidomics: Comprehensive Mass Spectrometry of Lipids (John Wiley & Sons), pp. 201–216.

Hannun, Y.A., and Obeid, L.M. (2018). Sphingolipids and their metabolism in physiology and disease. Nat. Rev. Mol. Cell Biol. *19*, 175–191.

Harvald, E.B., Olsen, A.S., and Færgeman, N.J. (2015). Autophagy in the light of sphingolipid metabolism. Apoptosis *20*, 658–670.

Haynes, C.A., Allegood, J.C., Park, H., and Sullards, M.C. (2009). Sphingolipidomics: methods for the comprehensive analysis of sphingolipids. J. Chromatogr. B Analyt. Technol. Biomed. Life Sci. *877*, 2696–2708.

Hla, T., and Kolesnick, R. (2014). C16:0-ceramide signals insulin resistance. Cell Metab. *20*, 703–705.

Hoene, M., Li, J., Häring, H.U., Weigert, C., Xu, G., and Lehmann, R. (2014). The lipid profile of brown adipose tissue is sex-specific in mice. Biochim. Biophys. Acta *1842*, 1563–1570.

Hornemann, T., Penno, A., Rütti, M.F., Ernst, D., Kivrak-Pfiffner, F., Rohrer, L., and von Eckardstein, A. (2009). The SPTLC3 subunit of serine palmitoyltransferase generates short chain sphingoid bases. J. Biol. Chem. *284*, 26322–26330.

Hruz, T., Laule, O., Szabo, G., Wessendorp, F., Bleuler, S., Oertle, L., Widmayer, P., Gruissem, W., and Zimmermann, P. (2008). Genevestigator v3: a reference expression database for the meta-analysis of transcriptomes. Adv. Bioinforma. *2008*, 420747.

Huttlin, E.L., Jedrychowski, M.P., Elias, J.E., Goswami, T., Rad, R., Beausoleil, S.A., Villén, J., Haas, W., Sowa, M.E., and Gygi, S.P. (2010). A tissue-specific atlas of mouse protein phosphorylation and expression. Cell *143*, 1174–1189.

Iseki, K. (2008). Gender differences in chronic kidney disease. Kidney Int. *74*, 415–417.

Jain, M., Ngoy, S., Sheth, S.A., Swanson, R.A., Rhee, E.P., Liao, R., Clish, C.B., Mootha, V.K., and Nilsson, R. (2014). A systematic survey of lipids across mouse tissues. Am. J. Physiol. Endocrinol. Metab. *306*, E854–E868.

Johnson, E.L., Heaver, S.L., Waters, J.L., Kim, B.I., Bretin, A., Goodman, A.L., Gewirtz, A.T., Worgall, T.S., and Ley, R.E. (2020). Sphingolipids produced by gut bacteria enter host metabolic pathways impacting ceramide levels. Nat. Commun. *11*, 2471.

Jojima, K., Edagawa, M., Sawai, M., Ohno, Y., and Kihara, A. (2020). Biosynthesis of the anti-lipid-microdomain sphingoid base 4,14-sphingadiene by the ceramide desaturase FADS3. FASEB J. *34*, 3318–3335.

Karsai, G., Lone, M., Kutalik, Z., Brenna, J.T., Li, H., Pan, D., von Eckardstein, A., and Hornemann, T. (2020). FADS3 is a Δ14Z sphingoid base desaturase that contributes to gender differences in the human plasma sphingolipidome. J. Biol. Chem. *295*, 1889–1897.

Kautzky-Willer, A., Harreiter, J., and Pacini, G. (2016). Sex and Gender Differences in Risk, Pathophysiology and Complications of Type 2 Diabetes Mellitus. Endocr. Rev. *37*, 278–316.

Kharel, Y., Huang, T., Salamon, A., Harris, T.E., Santos, W.L., and Lynch, K.R. (2020). Mechanism of sphingosine 1-phosphate clearance from blood. Biochem. J. *477*, 925–935.

Kim, S.N., Jung, Y.S., Kwon, H.J., Seong, J.K., Granneman, J.G., and Lee, Y.H. (2016). Sex differences in sympathetic innervation and browning of white adipose tissue of mice. Biol. Sex Differ. *7*, 67.

Laaksonen, R., Ekroos, K., Sysi-Aho, M., Hilvo, M., Vihervaara, T., Kauhanen, D., Suoniemi, M., Hurme, R., März, W., Scharnagl, H., et al. (2016). Plasma ceramides predict cardiovascular death in patients with stable coronary artery disease and acute coronary syndromes beyond LDL-cholesterol. Eur. Heart J. *37*, 1967–1976.

Laviad, E.L., Albee, L., Pankova-Kholmyansky, I., Epstein, S., Park, H., Merrill, A.H., Jr., and Futerman, A.H. (2008). Characterization of ceramide synthase 2: tissue distribution, substrate specificity, and inhibition by sphingosine 1-phosphate. J. Biol. Chem. *283*, 5677–5684.

Lee, H., German, J.B., Kjelden, R., Lebrilla, C.B., and Barile, D. (2013). Quantitative analysis of gangliosides in bovine milk and colostrum-based dairy products by ultrahigh performance liquid chromatography-tandem mass spectrometry. J. Agric. Food Chem. *61*, 9689–9696.

Li, M.H., Hla, T., and Ferrer, F. (2011). Sphingolipid modulation of angiogenic factor expression in neuroblastoma. Cancer Prev. Res. (Phila.) *4*, 1325–1332.

Luukkonen, P.K., Sädevirta, S., Zhou, Y., Kayser, B., Ali, A., Ahonen, L., Lallukka, S., Pelloux, V., Gaggini, M., Jian, C., et al. (2018). Saturated Fat Is

More Metabolically Harmful for the Human Liver Than Unsaturated Fat or Simple Sugars. Diabetes Care *41*, 1732–1739.

Martín-Timón, I., Sevillano-Collantes, C., Segura-Galindo, A., and Del Cañizo-Gómez, F.J. (2014). Type 2 diabetes and cardiovascular disease: Have all risk factors the same strength? World J. Diabetes *5*, 444–470.

Mayo, R., Crespo, J., Martínez-Arranz, I., Banales, J.M., Arias, M., Mincholé, I., Aller de la Fuente, R., Jimenez-Agüero, R., Alonso, C., de Luis, D.A., et al. (2018). Metabolomic-based noninvasive serum test to diagnose nonalcoholic steatohepatitis: Results from discovery and validation cohorts. Hepatol. Commun. *2*, 807–820.

Meikle, P.J., and Summers, S.A. (2017). Sphingolipids and phospholipids in insulin resistance and related metabolic disorders. Nat. Rev. Endocrinol. *13*, 79–91.

Merrill, A.H., Jr. (2011). Sphingolipid and glycosphingolipid metabolic pathways in the era of sphingolipidomics. Chem. Rev. *111*, 6387–6422.

Mielke, M.M., Haughey, N.J., Bandaru, V.V., Weinberg, D.D., Darby, E., Zaidi, N., Pavlik, V., Doody, R.S., and Lyketsos, C.G. (2011). Plasma sphingomyelins are associated with cognitive progression in Alzheimer's disease. J. Alzheimers Dis. *27*, 259–269.

Narayanaswamy, P., Shinde, S., Sulc, R., Kraut, R., Staples, G., Thiam, C.H., Grimm, R., Sellergren, B., Torta, F., and Wenk, M.R. (2014). Lipidomic "deep profiling": an enhanced workflow to reveal new molecular species of signaling lipids. Anal. Chem. *86*, 3043–3047.

Ngo, S.T., Steyn, F.J., and McCombe, P.A. (2014). Gender differences in autoimmune disease. Front. Neuroendocrinol. *35*, 347–369.

O'Brien, J.S., and Rouser, G. (1964). The fatty acid composition of brain sphingolipids: sphingomyelin, ceramide, cerebroside, and cerebroside sulfate. J. Lipid Res. *5*, 339–342.

Ohshima, T., Murray, G.J., Swaim, W.D., Longenecker, G., Quirk, J.M., Cardarelli, C.O., Sugimoto, Y., Pastan, I., Gottesman, M.M., Brady, R.O., and Kulkarni, A.B. (1997). alpha-Galactosidase A deficient mice: a model of Fabry disease. Proc. Natl. Acad. Sci. USA *94*, 2540–2544.

Palasca, O., Santos, A., Stolte, C., Gorodkin, J., and Jensen, L.J. (2018). TISSUES 2.0: an integrative web resource on mammalian tissue expression. Database (Oxford) *2018*, bay003.

Palmano, K., Rowan, A., Guillermo, R., Guan, J., and McJarrow, P. (2015). The role of gangliosides in neurodevelopment. Nutrients *7*, 3891–3913.

Palmisano, B.T., Zhu, L., Eckel, R.H., and Stafford, J.M. (2018). Sex differences in lipid and lipoprotein metabolism. Mol. Metab. *15*, 45–55.

Parks, B.W., Nam, E., Org, E., Kostem, E., Norheim, F., Hui, S.T., Pan, C., Civelek, M., Rau, C.D., Bennett, B.J., et al. (2013). Genetic control of obesity and gut microbiota composition in response to high-fat, high-sucrose diet in mice. Cell Metab. *17*, 141–152.

Pédrono, F., Blanchard, H., Kloareg, M., D'andréa, S., Daval, S., Rioux, V., and Legrand, P. (2010). The fatty acid desaturase 3 gene encodes for different FADS3 protein isoforms in mammalian tissues. J. Lipid Res. *51*, 472–479.

Pradas, I., Huynh, K., Cabré, R., Ayala, V., Meikle, P.J., Jové, M., and Pamplona, R. (2018). Lipidomics Reveals a Tissue-Specific Fingerprint. Front. Physiol. *9*, 1165.

Regitz-Zagrosek, V., Oertelt-Prigione, S., Prescott, E., Franconi, F., Gerdts, E., Foryst-Ludwig, A., Maas, A.H., Kautzky-Willer, A., Knappe-Wegner, D., Kintscher, U., et al.; EUGenMed Cardiovascular Clinical Study Group (2016). Gender in cardiovascular diseases: impact on clinical manifestations, management, and outcomes. Eur. Heart J. *37*, 24–34.

Régnier, M., Polizzi, A., Guillou, H., and Loiseau, N. (2019). Sphingolipid metabolism in non-alcoholic fatty liver diseases. Biochimie *159*, 9–22.

Rosell, M., Kaforou, M., Frontini, A., Okolo, A., Chan, Y.W., Nikolopoulou, E., Millership, S., Fenech, M.E., MacIntyre, D., Turner, J.O., et al. (2014). Brown and white adipose tissues: intrinsic differences in gene expression and response to cold exposure in mice. Am. J. Physiol. Endocrinol. Metab. *306*, E945–E964.

Rosqvist, F., Kullberg, J., Ståhlman, M., Cedernaes, J., Heurling, K., Johansson, H.E., Iggman, D., Wilking, H., Larsson, A., Eriksson, O., et al. (2019). Overeating Saturated Fat Promotes Fatty Liver and Ceramides Compared With Polyunsaturated Fat: A Randomized Trial. J. Clin. Endocrinol. Metab. *104*, 6207–6219.

Russo, S.B., Ross, J.S., and Cowart, L.A. (2013a). Sphingolipids in obesity, type 2 diabetes, and metabolic disease. Handb. Exp. Pharmacol. *2013*, 373–401.

Russo, S.B., Tidhar, R., Futerman, A.H., and Cowart, L.A. (2013b). Myristate-derived d16:0 sphingolipids constitute a cardiac sphingolipid pool with distinct synthetic routes and functional properties. J. Biol. Chem. *288*, 13397–13409.

Sales, S., Graessler, J., Ciucci, S., Al-Atrib, R., Vihervaara, T., Schuhmann, K., Kauhanen, D., Sysi-Aho, M., Bornstein, S.R., Bickle, M., et al. (2016). Gender, Contraceptives and Individual Metabolic Predisposition Shape a Healthy Plasma Lipidome. Sci. Rep. *6*, 27710.

Savica, R., Murray, M.E., Persson, X.M., Kantarci, K., Parisi, J.E., Dickson, D.W., Petersen, R.C., Ferman, T.J., Boeve, B.F., and Mielke, M.M. (2016). Plasma sphingolipid changes with autopsy-confirmed Lewy Body or Alzheimer's pathology. Alzheimers Dement. (Amst.) *3*, 43–50.

Schiffer, V., Santiago-Mujika, E., Flunkert, S., Schmidt, S., Farcher, M., Loeffler, T., Schilcher, I., Posch, M., Neddens, J., Sun, Y., et al. (2020). Characterization of the visceral and neuronal phenotype of 4L/PS-NA mice modeling Gaucher disease. PLoS ONE *15*, e0227077.

Schmelz, E.M., Crall, K.J., Larocque, R., Dillehay, D.L., and Merrill, A.H., Jr. (1994). Uptake and metabolism of sphingolipids in isolated intestinal loops of mice. J. Nutr. *124*, 702–712.

Shayman, J.A. (2018). Targeting Glucosylceramide Synthesis in the Treatment of Rare and Common Renal Disease. Semin. Nephrol. *38*, 183–192.

Spiegel, S., and Merrill, A.H., Jr. (1996). Sphingolipid metabolism and cell growth regulation. FASEB J. *10*, 1388–1397.

Spiegel, S., and Milstien, S. (2011). The outs and the ins of sphingosine-1-phosphate in immunity. Nat. Rev. Immunol. *11*, 403–415.

Su, A.I., Wiltshire, T., Batalov, S., Lapp, H., Ching, K.A., Block, D., Zhang, J., Soden, R., Hayakawa, M., Kreiman, G., et al. (2004). A gene atlas of the mouse and human protein-encoding transcriptomes. Proc. Natl. Acad. Sci. USA *101*, 6062–6067.

Subathra, M., Korrapati, M., Howell, L.A., Arthur, J.M., Shayman, J.A., Schnellmann, R.G., and Siskind, L.J. (2015). Kidney glycosphingolipids are elevated early in diabetic nephropathy and mediate hypertrophy of mesangial cells. Am. J. Physiol. Renal Physiol. *309*, F204–F215.

Sullards, M.C., Liu, Y., Chen, Y., and Merrill, A.H., Jr. (2011). Analysis of mammalian sphingolipids by liquid chromatography tandem mass spectrometry (LC-MS/MS) and tissue imaging mass spectrometry (TIMS). Biochim. Biophys. Acta *1811*, 838–853.

Taguchi, A., Maruyama, H., Nameta, M., Yamamoto, T., Matsuda, J., Kulkarni, A.B., Yoshioka, H., and Ishii, S. (2013). A symptomatic Fabry disease mouse model generated by inducing globotriaosylceramide synthesis. Biochem. J. *456*, 373–383.

Teijaro, J.R., Walsh, K.B., Cahalan, S., Fremgen, D.M., Roberts, E., Scott, F., Martinborough, E., Peach, R., Oldstone, M.B., and Rosen, H. (2011). Endothelial cells are central orchestrators of cytokine amplification during influenza virus infection. Cell *146*, 980–991.

Tonks, K.T., Coster, A.C., Christopher, M.J., Chaudhuri, R., Xu, A., Gagnon-Bartsch, J., Chisholm, D.J., James, D.E., Meikle, P.J., Greenfield, J.R., and Samocha-Bonet, D. (2016). Skeletal muscle and plasma lipidomic signatures of insulin resistance and overweight/obesity in humans. Obesity (Silver Spring) *24*, 908–916.

Triebl, A., Burla, B., Selvalatchmanan, J., Oh, J., Tan, S.H., Chan, M.Y., Mellet, N.A., Meikle, P.J., Torta, F., and Wenk, M.R. (2020). Shared reference materials harmonize lipidomics across MS-based detection platforms and laboratories. J. Lipid Res. *61*, 105–115.

Troupiotis-Tsaïlaki, A., Zachmann, J., González-Gil, I., Gonzalez, A., Ortega-Gutiérrez, S., López-Rodríguez, M.L., Pardo, L., and Govaerts, C. (2017). Ligand chain length drives activation of lipid G protein-coupled receptors. Sci. Rep. *7*, 2020.

Uhlén, M., Fagerberg, L., Hallström, B.M., Lindskog, C., Oksvold, P., Mardinoglu, A., Sivertsson, Å., Kampf, C., Sjöstedt, E., Asplund, A., et al. (2015). Proteomics. Tissue-based map of the human proteome. Science *347*, 1260419.

Veldhuizen, E.J.A., and Haagsman, H.P. (2000). Role of pulmonary surfactant components in surface film formation and dynamics. Biochimica et Biophysica Acta (BBA) - Biomembranes *1467*, 255–270.

Vesper, H., Schmelz, E.M., Nikolova-Karakashian, M.N., Dillehay, D.L., Lynch, D.V., and Merrill, A.H., Jr. (1999). Sphingolipids in food and the emerging importance of sphingolipids to nutrition. J. Nutr. *129*, 1239–1250.

Vutukuri, R., Koch, A., Trautmann, S., Schreiber, Y., Thomas, D., Mayser, F., Meyer Zu Heringdorf, D., Pfeilschifter, J., Pfeilschifter, W., and Brunkhorst, R. (2020). S1P d20:1, an endogenous modulator of S1P d18:1/$S1P_2$ -dependent signaling. FASEB J. *34*, 3932–3942.

Wang, X., Magkos, F., and Mittendorfer, B. (2011). Sex differences in lipid and lipoprotein metabolism: it's not just about sex hormones. J. Clin. Endocrinol. Metab. *96*, 885–893.

Wang, J.R., Zhang, H., Yau, L.F., Mi, J.N., Lee, S., Lee, K.C., Hu, P., Liu, L., and Jiang, Z.H. (2014). Improved sphingolipidomic approach based on ultra-high performance liquid chromatography and multiple mass spectrometries with application to cellular neurotoxicity. Anal. Chem. *86*, 5688–5696.

Wigger, L., Cruciani-Guglielmacci, C., Nicolas, A., Denom, J., Fernandez, N., Fumeron, F., Marques-Vidal, P., Ktorza, A., Kramer, W., Schulte, A., et al. (2017). Plasma Dihydroceramides Are Diabetes Susceptibility Biomarker Candidates in Mice and Humans. Cell Rep. *18*, 2269–2279.

Yu, R.K., Nakatani, Y., and Yanagisawa, M. (2009). The role of glycosphingolipid metabolism in the developing brain. J. Lipid Res. *50* (*Suppl*), S440–S445.

Zhao, L., Spassieva, S., Gable, K., Gupta, S.D., Shi, L.Y., Wang, J., Bielawski, J., Hicks, W.L., Krebs, M.P., Naggert, J., et al. (2015). Elevation of 20-carbon long chain bases due to a mutation in serine palmitoyltransferase small subunit b results in neurodegeneration. Proc. Natl. Acad. Sci. USA *112*, 12962–12967.

Zhao, J., Zhu, M., Jiang, H., Shen, S., Su, X., and Shi, Y. (2019). Combination of sphingosine-1-phosphate receptor 1 (S1PR1) agonist and antiviral drug: a potential therapy against pathogenic influenza virus. Sci. Rep. *9*, 5272.

Zhong, L., Kong, J.N., Dinkins, M.B., Leanhart, S., Zhu, Z., Spassieva, S.D., Qin, H., Lin, H.P., Elsherbini, A., Wang, R., et al. (2018). Increased liver tumor formation in neutral sphingomyelinase-2-deficient mice. J. Lipid Res. *59*, 795–804.

Zitomer, N.C., Mitchell, T., Voss, K.A., Bondy, G.S., Pruett, S.T., Garnier-Amblard, E.C., Liebeskind, L.S., Park, H., Wang, E., Sullards, M.C., et al. (2009). Ceramide synthase inhibition by fumonisin B1 causes accumulation of 1-deoxysphinganine: a novel category of bioactive 1-deoxysphingoid bases and 1-deoxydihydroceramides biosynthesized by mammalian cell lines and animals. J. Biol. Chem. *284*, 4786–4795.

Zuellig, R.A., Hornemann, T., Othman, A., Hehl, A.B., Bode, H., Güntert, T., Ogunshola, O.O., Saponara, E., Grabliauskaite, K., Jang, J.H., et al. (2014). Deoxysphingolipids, novel biomarkers for type 2 diabetes, are cytotoxic for insulin-producing cells. Diabetes *63*, 1326–1339.

STAR★METHODS

KEY RESOURCES TABLE

REAGENT or RESOURCE	SOURCE	IDENTIFIER
Chemicals, peptides, and recombinant proteins		
All internal lipid standards for quantitative lipidomics	Avanti Polar Lipids	https://avantilipids.com/divisions/lipidomics/lipid-maps-ms-standards
Standard chow	Provimi Kliba AG, Kaiseraugst	#3432
60% calories from fat high-fat diet	Kliba-Nafag	#2127
Deposited data		
Lipidomic datasets of tissues and plasma analyzed	https://dx.doi.org/10.17632/gbgm9bscph.1	Data S1
Experimental models: Organisms/Strains		
C57BL/6	The mice used in this study were bred in-house	#000664
Software and algorithms		
GraphPad Prism 8	GraphPad Software, Inc	https://www.graphpad.com/
R	R Core Team	https://www.R-project.org/
Genevestigator	Hruz et al., 2008	N/A
MetaboAnalyst	https://www.metaboanalyst.ca/home.xhtml	N/A
Agilent MassHunter Quantitative Analysis Software Version 8	Agilent	N/A
Agilent MassHunter Data Acquisition Software	Agilent	N/A
Other		
Agilent 6495 Triple Quadrupole LC/MS system	Agilent	N/A
1290 Infinity II High-Throughput System	Agilent	N/A

RESOURCE AVAILABILITY

Lead contact

Further information and requests for resources and reagents should be directed to and will be fulfilled by the Lead Contact, Federico Torta (bchfdtt@nus.edu.sg).

Materials availability

This study did not generate new unique reagents.

Data and code availability

Figures D1 to D5; Tables D1 to D3 are deposited as Data S1 in Mendeley Data, https://dx.doi.org/10.17632/gbgm9bscph.1. The raw data and R scripts are available on Mendeley data. https://dx.doi.org/10.17632/gbgm9bscph.1

EXPERIMENTAL MODEL AND SUBJECT DETAILS

Male and female C57BL/6 wild-type mice 16 weeks old were caged individually and maintained in a 12:12 (light:dark) cycle at (temperature) and (humidity). The mice were fed *ad libitum* with a chow diet (KLIBA #3432). The existence of a rhythmicity of plasma and platelet SP metabolism, likely mediated by melatonin, has been shown to be present in some strains of rodents. However, as C57BL/6 mice do not produce melatonin, in our model there should not be any circadian variation of the sphingolipidome. Six females and five males were sacrificed by CO2 inhalation and twenty-one tissues were collected. Hippocampus, cerebellum, cortex, lung, heart, spleen, kidney, liver, stomach, large intestine, small intestine, brown adipose tissue (BAT), subcutaneous white adipose tissue

(sub-WAT), epididymal white adipose tissue (epiWAT), testis, ovary, muscle (quadriceps), thymus, lymph nodes (inguinal) and skin (from the back), were washed few times with ice cold PBS and snap frozen in liquid nitrogen post dissection. As all the tissues were washed in PBS without perfusion, and as remnant red blood cells containing SP (especially S1P) might still be present, we cannot exclude their potential interference on SP measurements. For plasma, blood from vena cava was collected in Li-heparin coated tube to prevent coagulation, and centrifuged at 4 degrees and 2500 g for 15 min, the supernatant was collected. For the high-fat diet study, eight male mice were fed with chow diet (KLIBA #3432) and eight male mice were fed with high-fat diet (60% kcal % fat NAFAG 2127 from KLIBA). The mice were fed with HFD from the age of 6 weeks for 10 weeks. The body weights at the time of sacrifice are provided (Data S1, Table D3). All the procedures followed the protocols approved by the Kantonales Veterinäramt of the Kanton Basel-Stadt.

METHOD DETAILS

Lipid extraction

The extraction solvent was prepared by dissolving the following lipid standards in butanol:methanol (1:1): Ceramide d18:1/8:0 (Avanti Polar Lipids, 860508) at 23.5 μmol/L, Glucosylceramide d18:1/8:0 (Avanti Polar Lipids, 860540) at 17 μmol/L, SM d18:1/6:0 (Avanti Polar Lipids, 860582) at 35.5 μmol/L, sphingosine d18:1 d7 (Avanti Polar Lipids, 860657) at 8.2 μmol/L, sphinganine d18:0 d7 (Avanti Polar Lipids, 860658) at 8.1 μmol/L, S1P d18:1 13C2D2 (Toronto Research Chemicals, S681502) at 5.2 μmol/L. Lipids were extracted using a single phase butanol:methanol method (Alshehry et al., 2015), where ~30 mg of tissue were homogenized in 1 mL extraction buffer using an Omni bead ruptor elite bead mill homogenizer (SKU:19-649S- Omni International). Wet weight values were only used during the first phase of the lipid extraction, while for normalization purposes the final dry weight was used. The homogenate was vortexed for 30 s and sonicated for 30 min. After sonication, the samples were centrifuged for 10 min at 14,000 g and the supernatant containing the sphingolipids was transferred to the MS vials for targeted sphingolipidomics. The pellet was dried in a speedvac and the dry weight was estimated. For ovary, wet weight was used for normalization. For the adipose tissue, the tissues were not completely dry even after overnight processing, hence partial dry weight was used to normalize the lipid levels. Technical quality controls (TQC) were prepared for each tissue by pooling extracts from all the samples of the same tissue. Each tissue was extracted and analyzed as a batch. TQCs were injected at the beginning and at the end of each batch. A TQC was also injected every 5 samples.

For S1P analysis, 90 μL of lipid extract were transferred to a fresh tube and dried in a speed vac. The dried lipid extract was resuspended in 90 μL of methanol. Twenty microliters of (Trimethylsilyl) diazomethane 2M in hexane (e.g., #AC385330250, ACROS Organics) solution were added and the samples were placed in a thermomixer at 25°C, 700 rpm for 20 min. The derivatization reaction was arrested using 1 μL of acetic acid solution (Narayanaswamy et al., 2014). Forty microliters of derivatized lipid extract from each sample were transferred to each vial for LC-MS analysis.

Targeted lipidomics

A targeted sphingolipidomic analysis was performed using an LC ESI-QQQ MS/MS system in MRM mode. For the mouse atlas 114 sphingolipids were quantified, including 4 SPH, 43 Cer, 32 HexCer, 13 Hex2Cer, 8 GM3, 25 SM. The chromatographic separation was performed on an Agilent ZORBAX Eclipse plus Rapid Resolution HD C18 (95 Å, 2.1 × 50 mm, 1.8 μm) column, thermostatted at 40°C in an Agilent 1290 UHPLC system. The flow rate was 400 μL min-1 with solvent A composed of 10 mM ammonium formate in water-acetonitrile (60:40, v/v) and solvent B composed of 10 mM ammonium formate in isopropanol-acetonitrile (90:10, v/v). Mobile Phase A and B were mixed to create the following gradient: 20% B at 0 min raised to 60% B at 2.00 min, further raised to 100% B at 7.00 min, maintained at 100% B until 9.00 min, and re-equilibrated with 20% B from 9.01 min to 10.80 min. The total run time was 10.80 min.

The UHPLC was connected to an Agilent 6495 QQQ MS (Agilent Technologies, Santa Clara, USA). The AJS ESI source parameters were the following: dry gas temperature and flow were 200°C and 12 L min-1 respectively, nebulizer pressure 25 psi, sheath gas temperature and flow were set to 250°C and 12 L min-1 respectively, capillary voltage and nozzle voltage set to 3500 V and 500 V respectively, and the delta EMV was 200 V. Positive high/low pressure RF was set to 80/40 and negative high/low pressure RF was 150/60. Retention time windows were set to 1 min and the cycle time to 600 ms. The fragmentor and cell acceleration voltage were set to 380 V and 5 V respectively. The collision energy varied based on the lipid class. Two microliters of tissue extract were injected for analysis. The MS was operated in both positive and negative ionization modes and a dynamic multiple reaction monitoring method (dMRM) was set up for the analysis. For each SP molecular species more than one transition was measured; the transition with the highest response was used as a quantifier and the transition with a lower response was used as a qualifier. The method included 364 transitions, with 151 transitions for quantifiers and 213 transitions for qualifiers. The retention time and co-eluting qualifier peaks served as a reference to confirm the identity of the lipid. For some species, more than one qualifier was included to improve the identification of the sphingolipid. However, in certain low abundant lipids and some molecular species of the SM class, the peaks were identified only based on retention times and the quantifier, as the signal of the qualifier was not detectable.

The fragmentation patterns of SP have been previously described (Han, 2016; Lee et al., 2013; Narayanaswamy et al., 2014; Zitomer et al., 2009). For Cer, HexCer and Hex2Cer the product ion corresponds to the characteristic SPH. For d18:1, d18:2 and

d16:1 containing SP the product ions are m/z 264, 262 and 236 respectively. Product ions may be generated from either the intact precursor $[M+H]^+$ or the precursors that underwent a water loss $[M\text{-}H_2O+H]^+$ in the ion source. $[M\text{-}H_2O+H]^+$ > SPH (264/262/236) was used as the quantifier for Cer while for HexCer and Hex2Cer, "$[M+H]^+$ > SPH (264/262/236)" was used as the quantifier. For GM3, the SPH product ion was measured in positive mode and another product ion at m/z 290.2, corresponding to the sialic acid fragment, was measured in negative mode. $[M+H]^+$ > SPH (264/262/236) was used as a quantifier for GM3. For sphingomyelins (SM), m/z 184.1 corresponding to the phosphocholine was used as a quantifier and the SPH product ion was used as a qualifier. For the SPHs, three product ions were measured, a water loss of one water molecule $[M\text{-}H_2O+H]^+$, another ion generated due to water loss of two water molecules $[M\text{-}2(H_2O)+H]^+$ and a third product ion generated from the neutral loss of 48.0 amu corresponding to the losses of a water molecule and a formaldehyde. The transition $[M+H]^+$ > $[M\text{-}H_2O+H]^+$ was used as the quantifier for d18:1, d18:2 and d16:1. For SPH d18:0, along with the three transitions reported for other SPHs, another fragment at m/z 60, corresponding to $[NH_2OH]^+$, was used as the quantifier.

Sphingoid base-1-phosphates (S1P) analysis

The S1Ps, among which S1P d18:1 is well known, were analyzed using HILIC electrospray ionization mass spectrometry. Chromatographic separation was performed on a Waters ACQUITY UPLC BEH HILIC (130 Å, 2.1 × 100 mm, 1.7 μm) column thermostatted at 60°C in an Agilent 1290 UHPLC system. For mobile phase preparation, a 25 mM Ammonium formate buffer was prepared by dissolving 1575 mg ammonium formate in 800 mL milliQ water and 100 μL formic acid were used to adjust the pH to 4.6. The volume was then adjusted to 1 L with MilliQ water. The flow rate was 400 μL min-1 with mobile phase A composed of acetonitrile-25 mM ammonium formate buffer (50:50, v/v) and mobile phase B composed of acetonitrile-25 mM ammonium formate buffer (95:5, v/v). Mobile phase A and B were mixed to create the following gradient: 99.90% B at 0 min to 40% B at 5.00 min, 10% B at 6.50 min and re-equilibrated at 99.90% B from 6.60 min to 9.60 min. The total run time was 9.60 min. An Agilent 1290 UHPLC system and the Agilent 6495 QQQ MS were used for these measurements. The AJS ESI source parameters for the MS were: dry gas temperature and flow were 200°C and 12 L min-1 respectively, nebulizer pressure 25 psi, sheath gas temperature and flow were set to 400°C and 12 L min-1 respectively, capillary voltage and nozzle voltage set to 3500 V and 500 V respectively, and the delta EMV was 200 V. Positive high/low pressure RF was set to 200/110.

The MS was operated in positive ionization mode and a multiple reaction monitoring method (MRM) was used for the analysis. The method included 30 transitions, with 15 transitions for quantifiers and 15 for qualifiers. For each S1P, two product ions at m/z 60.08 (quantifier) and m/z 113 (qualifier) generated from the TMS derivatized tetra-methylated form of S1P were monitored. The fragmentor, collision energy and cell acceleration voltage were set to 380 V, 29 V and 3 V respectively. 2 μL of derivatized tissue extract were injected for S1P analysis.

QUANTIFICATION AND STATISTICAL ANALYSIS

LC-MS/MS data analysis

The acquired MS data were analyzed using Agilent MassHunter software version B.08.00. R-packages, Metaboanalyst (Chong et al., 2018, 2019; Chong and Xia, 2020) and Prism software were used for the data visualization.

Normalization and quantification

The signal to noise ratios (S/N) were calculated using the raw peak areas in study samples and processed blanks (PBLK) as described in (equation *1*). Lipids that had S/N < 10 were eliminated from the analysis.

$$\frac{S}{N}(lipid\ x) = \frac{Average\ peak\ area\ for\ lipid\ x\ in\ Tissue\ QCs}{Average\ peak\ area\ for\ lipid\ x\ in\ PBLK} \quad \text{(equation 1)}$$

Internal standards were used to normalize the raw peak areas using corresponding quantifier/qualifier transitions. Cer were normalized to the internal standard Cer d18:1/8:0; HexCer, Hex2Cer and GM3 were normalized to HexCer d18:1/8:0; SM were normalized to SM d18:1/6:0; SPH d18:1, SPH d18:2 and SPH d16:1 were normalized to SPH d18:1 d7; SPH d18:0 was normalized to SPH d18:0 d7; S1P were normalized to S1P d18:1 13C2, D2. Normalized values to IS (V1) were calculated as described in (equation 2)

$$V1(lipid\ x) = \left(\frac{Peak\ area\ for\ lipid\ x\ in\ sample\ y}{Peak\ area\ of\ corresponding\ IS\ in\ sample\ y}\right) \times Concentration\ of\ ISTD \quad \text{(equation 2)}$$

CoVs of the lipids were calculated after normalization as

$$\%CoV\ (\text{lipid x}) = \left(\frac{\text{Stdev of V1(lipid x)in all Tissue QCs}}{\text{Average of V1(lipid x)in all Tissue QCs}}\right) \times 100 \quad \text{(equation 3)}$$

Lipids that showed a % CoV > 30 were eliminated in further analysis.

Concentrations were calculated after normalization to IS and were further normalized to the dry weight of the tissue. Final sphingolipid levels in the tissue were reported as nmol of lipid per g of dry tissue.

$$V2(lipid\ x) = \left(\frac{V1}{dry\ weight\ of\ sample\ y(g)}\right) \quad \text{(equation 4)}$$

Due to the methodology used in our study we are not able to report absolute concentration values. Endogenous species were quantified using one standard per lipid class thus our method can only deliver relative quantitation results.

Absolute quantification was only done for S1P d18:1 as a corresponding labeled standard was available, while for all other species a semiquantitative approach based on class-specific standards was used.